

System-level Utilization of Low-grade, MW-scale Thermal Loads for Electric Aircraft

Andrew Scott White*

Massachusetts Institute of Technology, Cambridge, Massachusetts 02139

Elias Waddington[†], Jason M. Merret[‡], and Phillip J. Ansell[§]
University of Illinois at Urbana-Champaign, Urbana, Illinois 61801

Edward M. Greitzer[¶]

Massachusetts Institute of Technology, Cambridge, Massachusetts 02139

David K. Hall^{||}

Pennsylvania State University, University Park, Pennsylvania 16802

This paper describes the analysis of a hydrogen fuel-cell-powered transport-category aircraft, similar in mission performance to a Boeing 737-800. The configuration examined produced peak waste heat loads up to 16 megawatts. Contemporary thermal dissipation systems, such as radiators, lead to a substantial drag contribution due to the large cooling surfaces required. In the paper, we 1) characterize the magnitude, occurrence, and effect of the thermal management challenge for fuel-cell-powered civil air transport, as exemplified through the CHEETA aircraft; 2) investigate multiple thermal management strategies that leverage thermal energy deposition from waste heat sources as a contribution within the propulsion system; and 3) demonstrate the impact of applying one of those strategies to enhance aircraft performance. We show that thermal system design for MW-scale electric aircraft cannot be considered as a simple drag penalty to be quantified after preliminary design is complete: power, propulsion, and thermal systems must be designed together.

I. Nomenclature

Variables and Abbreviations

A_m	=	fuel cell membrane area
A_r, A_s	=	radiator face area and surface area
AR	=	wing aspect ratio
α	=	HEX-fan face area ratio
C_c and C_h	=	cold- and hot-side fluid heat capacity
C_d	=	nacelle drag coefficient
C_{min} and C_{max}	=	minimum and maximum fluid heat capacity
C_p	=	specific heat capacity
C_x	=	net axial force coefficient
D_{core}	=	net force balance of HEX core due to friction and heat addition
$D_{nacelle}$	=	skin-friction force on the nacelle external surface
D_{weight}	=	aircraft drag incurred by the added heat exchanger weight
e	=	cell voltage
e_o	=	open-circuit reference cell voltage

*Graduate Research Assistant, Department of Aeronautics and Astronautics, AIAA Member

[†]Graduate Research Assistant, Department of Aerospace Engineering, AIAA Member

[‡]Clinical Associate Professor, Department of Aerospace Engineering, AIAA Associate Fellow

[§]Associate Professor, Department of Aerospace Engineering, AIAA Senior Member

[¶]H.N. Slater Professor, Department of Aeronautics and Astronautics, AIAA Honorary Fellow

^{||}Assistant Professor, Department of Aerospace Engineering, AIAA Member

ϵ	=	heat exchanger effectiveness
F	=	Faraday's constant
ΣF_x	=	net axial force
FC	=	fuel cell
Δg_f	=	Gibb's energy of formation for water
γ	=	specific heat ratio for air
i	=	fuel cell current
i_d	=	fuel cell current density
i_{int}	=	internal fuel cell current
g	=	gravitational acceleration constant
HEX	=	heat exchanger
h_{fuel}	=	fuel heating value
η	=	efficiency
K_f	=	non-dimensional friction coefficient
K_h	=	non-dimensional heat transfer coefficient
K_p	=	mechanical flow power coefficient
L/D	=	lift-to-drag ratio
\dot{m}	=	mass flow rate
M	=	Mach number
MM_H	=	molar mass of hydrogen
$MTOW$	=	maximum take-off weight
N_c	=	number of fuel cells in a stack
N_{TU}	=	number of heat transfer units
OEW	=	operational empty weight
OML	=	outer mold line
PEM	=	proton exchange membrane
ψ	=	HEX weight scaling factor
P	=	static pressure
Pr	=	Prandtl number
Φ	=	HEX non-dimensional pressure drop parameter
\dot{Q}	=	thermal load per stack
R	=	universal gas constant
ρ	=	air density
S	=	wing surface area
σ	=	blockage factor
T	=	temperature
U_{avg}	=	average convective heat transfer coefficient
u	=	velocity
μ_{fuel}	=	fuel utilization factor
\dot{W}	=	power

Subscripts

∞	=	ambient or freestream
1, 2, ...	=	station numbers
fc	=	fuel cell
p	=	primary
r	=	radiator
s	=	secondary
t	=	stagnation

II. Introduction

FOR many electrified and fully-electric aircraft concepts, large amounts of waste heat are generated by propulsive power components such as batteries [1], fuel cells [2], power transmission cables, power electronics, and electric machines [3]. Thermal management and utilization of waste heat is therefore an important issue for these configurations [4–6].

Potential solutions to address this issue depend on the quality and magnitude of the waste heat thermal load. Quality (or grade) refers to the temperature of the rejected heat. High-temperature waste heat is more easily utilized, and therefore higher grade, than low-temperature heat. For example, high-quality heat (1,400°C) produced via combustion in aero-engines directly generates thrust power via an exhaust jet [7]. For low-quality heat (80°C), uses are limited to utilities such as wash water heating, wing de-icing, and fuel pre-heating [8]. In this work, we consider the thermal loads associated with high-temperature proton exchange membrane fuel cells, which operate at temperatures up to 200°C [9].

The thermal load magnitude also dictates what solutions are practical. For a turbo-electric aircraft such as the STARC-ABL concept [10], the kW-scale thermal loads could be managed by outer mold line (OML) heat exchangers [11]. The limits on the available aircraft surface area, make this strategy impractical as the sole solution for the MW-scale thermal loads of a fuel-cell-powered aircraft such as CHEETA [12]. Conventional radiator-type cooling systems introduce substantial parasitic drag penalties, mainly due to skin friction on additional ducting and radiator surface area [12]. An avenue to mitigate the penalties, however, is through utilizing the waste heat from the fuel cell to produce thrust [13]. The heat addition in a ducted radiator creates thrust, as in a ramjet [7], as has been quantified through combined heat transfer and internal flow analyses [14, 15].

In the following sections, we provide a conceptual overview of the aircraft and fuel cell systems, present a thermal management solution to address CHEETA-like applications, quantify the impact of that thermal system on aircraft-level performance, and discuss multiple integrated thermal system architectures and their potential benefits.

III. CHEETA Aircraft Concept

The CHEETA aircraft concept was developed through the Center for High-Efficiency Electrical Technologies for Aircraft (CHEETA) to address Boeing 737-800 mission performance and requirements with zero carbon dioxide (CO_2) and nitrogen oxide (NO_x) emissions in flight [12]. The configuration, as sketched in Figure 1, is a high-wing, V-tail, 180-passenger, single-aisle, transport-category aircraft. Nine electric motor-driven fans, with three sets of propulsors over each wing and at the aft section of the fuselage, provide thrust for the vehicle. The right-hand side of the figure depicts the major internal systems of the aircraft. Fuel cells, in green, are located near the propulsors, to shorten the distance between electrical generation and usage. This proximity is also convenient for thermal system integration; the motors, inverters, and electrical transmission lines are cooled by the cryogenic liquid-hydrogen fuel [3].

The parameters for a baseline CHEETA configuration are listed in Table 1, reflecting improvements to climb speed scheduling, propulsive and aerodynamic models, and electrical transmission architecture since the initial study [12]. A key finding from that study was that increasing the number of fuel cell stacks decreases fuel consumption and time to climb. For example, if the aircraft shown in Figure 1 were sized for a 15% higher maximum power, the fuel cell stacks would be 23.7% heavier but net fuel weight would be reduced by 5.6%. This process, referred to as "oversizing" the power system, takes advantage of stack efficiency scaling inversely with power during cruise operation [16]. In Section IV, we apply this idea to further investigate fuel consumption reductions.

Table 1 CHEETA aircraft specifications for a nominal fuel cell configuration

Aircraft Parameter	Nominal
AR	10
Wing Area	1,840 ft^2
Wing Span	136 ft
OEW	138,580 lb
MTOW	190,450 lb
Fuel Weight	16,870 lb
Fuel Cell Weight	20,070 lb
Fuel Cell Maximum Power	22 MW

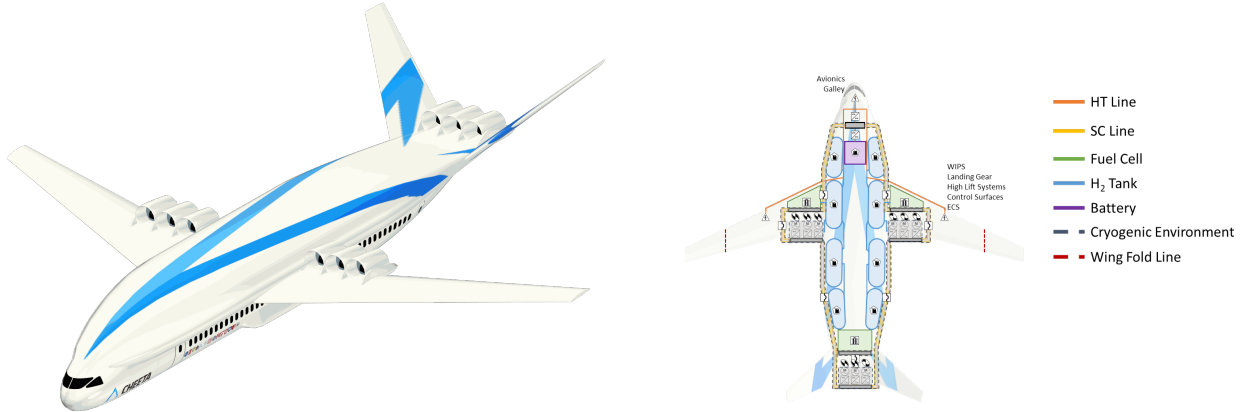


Fig. 1 Isometric view (left) and system overview (right) of CHEETA aircraft concept

A. PEM Fuel Cell Power System

Proton exchange membrane (PEM) fuel cells generate electrical power by combining hydrogen (H_2) fuel at the anode and ambient oxygen (O_2) at the cathode to form water [16]. At the catalyzed membrane surface, protons (H^+) pass through the membrane while electrons (e^-) pass through the circuit connecting the electrodes. For an ideal fuel cell, the voltage is governed by the Gibbs free energy of formation for water at standard pressure (1 bar), as in Equation 1, and the current is governed by the fuel flow rate, in Equation 2: these expressions represent the open-circuit cell voltage (e_o) and internal current (i_{int}) of the fuel cell, respectively [16]. Fuel cells can be combined in series to form stacks of higher voltage (equal to the number of cells times cell voltage) and in parallel for increased power output at a fixed voltage.

$$e_o = \frac{-\Delta g_f}{2F} \quad (1)$$

$$i_{int} = 2F \times \frac{\dot{m}_{fuel}}{N_c} \times \frac{1mol}{2(MM_H)} \quad (2)$$

$$i_d = \frac{i_{int}}{A_m} = \frac{i}{\mu_{fuel} A_m} \quad (3)$$

The cell voltage can be adjusted for various operating conditions using the Nernst equation as described in [16] and shown in equation 4,

$$e = e_o + \frac{RT}{2F} \times \ln \frac{cH_2 P_{fuel} \sqrt{cO_2 P_{air}}}{cH_2 O P_{H_2 O}} \quad (4)$$

where R is the universal gas constant (8.314 J/mol-K), cX is the mixing ratio of each species X , and e is the cell voltage. This equation captures voltage variations due to changes in operating temperature T , species mixing ratio cX , and partial pressure P [16].

In practice, several mechanisms limit fuel cell operation [16–19]:

- 1) Ohmic losses, related to the electrical resistance of the fuel cell and circuits
- 2) Activation losses, related to the chemical kinetics at the anode and cathode surfaces
- 3) Mass transport losses, related to the non-ideal transport of reactants or products to or from the electrodes
- 4) Fuel crossover and short-circuiting, related to the loss of energy from wasted fuel or electrons

Each of these loss mechanisms reduces the output power, and therefore the efficiency, of the fuel cell (see Appendix for details). We assume that all fuel energy not producing electrical power (\dot{W}_{fc}) produces heat in the fuel cell, which will be sent to a thermal management system at a temperature equal to the stack operating temperature. These losses are characterized by the fuel cell efficiency (η_{fc}), resulting in a thermal load (\dot{Q}).

$$\dot{Q} = \left(\frac{1 - \eta_{fc}}{\eta_{fc}} \right) \dot{W}_{fc} \quad (5)$$

We have applied this fuel cell performance model to the CHEETA power system based on high-temperature PEM fuel cell forecasts described in Waddington *et al* [12], with our projection of stack specific power based on these forecasts and industry press releases [20, 21]. The model parameters and resulting cell performance are presented in Figure 2, which shows cell voltage, efficiency, and power density at varied current density for a PEM fuel cell power system operating at an altitude of 37,000 feet. The y-intercept of cell voltage is set by the fuel crossover losses, which cause an idle voltage that is less than the open-circuit reference voltage. The non-linearities at low current densities are due to activation losses. The linear portion of the curve is driven by the ohmic losses, up until the precipitous decrease in voltage due to non-ideal mass transport [16]. The plot shows that fuel cell efficiency decreases with increasing power. For the 22 MW maximum power specified in Table 1, the fuel cell power system operates at 58% efficiency and produces 15.9 MW of waste heat. At cruise conditions, however, the power required is approximately 14 MW, corresponding to 62% efficiency and 8.5 MW of waste heat.

Parameter	Value
Stack specific power	2.7 kW/kg
Cell membrane area	446 cm ²
Number of cells per stack	1080
Fuel heating value	120 MJ/kg
Cell internal resistance	0.062 Ω – cm ²
Charge transfer coefficient	0.50
Exchange current density	10 ⁻⁵ – 10 ⁻³ A/cm ²
Fuel utilization coefficient	0.96
Operating Temperature	180 °C
Hydrogen fuel pressure	5 bar
Air compressor efficiency	0.90
Fraction of oxygen in air	0.21
Fraction of hydrogen in fuel	1.00

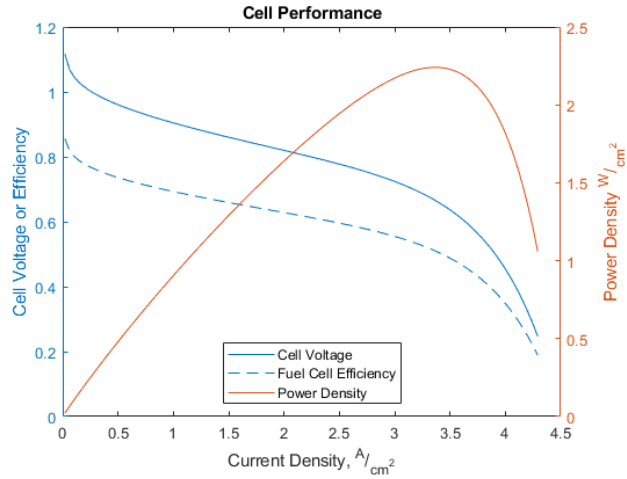


Fig. 2 Fuel cell parameters and performance are shown for varied current density to highlight the impact of the various loss mechanisms for the CHEETA fuel cell system.

B. Ducted Heat Exchanger Thermal System

To utilize fuel cell waste heat necessitates a ducted radiator heat exchanger (HEX). We quantify the HEX performance, following the methodology of Kays and London [14], using the effectiveness (ϵ) of a HEX based on the number of heat transfer units (N_{TU}), defined in Equations 6 and 7, respectively, for a counterflow liquid-air heat exchanger. In these relations, C_h and C_c are the hot and cold fluid capacity rates ($\dot{m}C_p$), respectively, and C_{min} and C_{max} refer to the smaller and larger of these two quantities. For the thermal systems considered, we assume polyethylene glycol ($C_p \approx 2200$ J/kg-K) to be the hot working fluid [22] and ambient air to be the cold fluid.

$$\epsilon = f\left(N_{TU}, \frac{C_h}{C_c}\right) = \frac{1 - e^{-N_{TU}(1-C_{min}/C_{max})}}{1 - (C_{min}/C_{max})e^{-N_{TU}(1-C_{min}/C_{max})}} \quad (6)$$

$$N_{TU} = \frac{A_s U_{avg}}{C_{min}} \quad (7)$$

To quantify the drag of such a heat exchanger in isolation, we rely on the combined heat transfer and internal flow analysis presented by Drela [15]. The HEX core drag contribution (D_{core}) refers to only the net drag of the core flow, defined as the airflow captured in the nacelle, sent through the HEX, and expelled through the outlet, as in Figure 3. The HEX drag power is estimated from Equation 8, which includes effects of friction and heat addition. Friction manifests as a pressure drop, as in Equation 9. The deposition of heat into the working fluid produces a density change, and an acceleration, as in Equation 10. If the resulting drag force is negative, it will be referred to as a HEX thrust. If K_f , K_h , and σ are known from empirical or numerical analysis, parameters K_f , K_h , and σ can be used directly in Equation 8; otherwise, Drela gives a representative value for typical liquid-air heat exchangers, as defined in Equation 11.

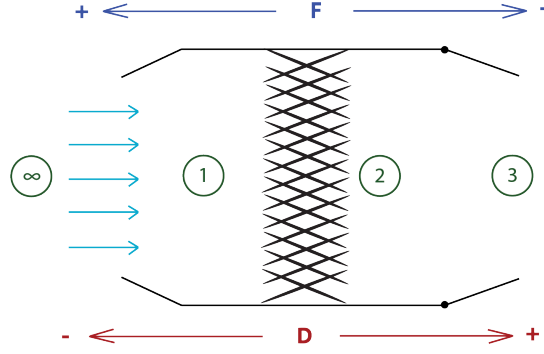


Fig. 3 Notional 1-D flow representation of an isolated ducted heat exchanger

$$\frac{D_{core} u_{\infty}}{\dot{Q}} = \left[\frac{u_{\infty}^2 P r^{2/3}}{c_p (T_r - T_{t1})} \frac{1}{\sigma^2} \frac{K_f}{K_h} \left(\frac{u_1}{u_{\infty}} \right)^2 - \frac{\gamma - 1}{2} M_{\infty}^2 \right] \quad (8)$$

$$\Delta P_{HEX} = \frac{1}{2} \rho_1 u_1^2 \Phi \quad (9)$$

$$\frac{u_2}{u_1} = \frac{\rho_1}{\rho_2} \approx \frac{T_2}{T_1} \quad (10)$$

$$\frac{1}{\sigma^2} \frac{K_f}{K_h} = 10 \quad (11)$$

The drag power relationship in Equation 8 strongly depends on the HEX face velocity, u_1 , which is controlled by a variable-area exhaust, based on the mass flow rate required for cooling the fuel cell stack. We determine u_1 for a specified heat load (\dot{Q}) and radiator face area (A_r) at a given flight state using Equation 12. We can then characterize HEX performance and drag based on empirical HEX effectiveness (ϵ) curves (Equation 6) provided in [14].

$$\frac{\dot{Q}_{HEX}}{\epsilon C_p (T_r - T_{t1})} = \dot{m}_{air} = u_1 A_r \rho_1 = u_1 A_r \rho_{\infty} \left(1 + \frac{\gamma - 1}{2} M_{\infty}^2 \right)^{\frac{1}{\gamma - 1}} \quad (12)$$

T_{t1} is determined using the following stagnation temperature relationship ($u_1 \ll u_{\infty}$) [23]:

$$T_{t1} \approx T_{t\infty} = T_{\infty} \left(1 + \frac{\gamma - 1}{2} M_{\infty}^2 \right) \quad (13)$$

From the core drag relationships above, it would appear desirable to increase the HEX frontal area (A_r) to slow down the flow and reduce core drag. This change, however, creates increased drag on the duct inlet surface, which we refer to as *nacelle drag*. This nacelle drag can be quantified using an empirical drag coefficient (C_d) for a specified flight condition [24]; we assume here a C_d of 0.04 at all conditions.

$$D_{Nacelle} u_{\infty} = \frac{C_d}{2} \rho_{\infty} u_{\infty}^3 A_r \quad (14)$$

The use of a heat exchanger also entails a weight addition. We assume the weight scales linearly with face area as given by Boeing [25] to account for the HEX, plumbing, valves, and coolant circulation pumps. The added weight requires additional lift, thus an associated drag which we denote as *weight drag*. The drag contribution is small relative to the force contributions of the core and nacelle.

$$D_{Weight} u_{\infty} = \frac{\psi A_r g u_{\infty}}{(L/D)} \quad (15)$$

The sum of the drag contributions result in a drag power which is used to quantify the total *thermal system drag* at a given flight velocity. The optimal system is achieved by balancing the different drag sources with the thrust requirement at the cruise point.

IV. Aircraft Performance Results

To characterize the impact of heat utilization on aircraft performance, the ducted HEX model (denoted as the isolated HEX) has been implemented into the sizing methods used to create the CHEETA configuration. The HEX-to-fan face area ratio is given as $A_r = \alpha A_{fan}$. Thermal system weight was estimated using the HEX weight scaling factor ($\psi = 11 \text{ lb}/ft^2$) [25] and Roskam's method for turbojet nacelle weight estimation (to account for the fairing and structure around the radiator) [26]. The nacelle weight estimate is conservative, since Roskam's method accounts for systems not included in a HEX nacelle.

A configuration with an aspect ratio (AR) of 10 and a wing planform area (S) of $1,840 \text{ ft}^2$ was selected as a representative case to characterize the impact of HEX design on aircraft-level performance, with α -values ranging from 0.5 to 2.0. The resulting MTOWs are shown in Figure 4. Configurations that did not close were removed, curtailing the α -space to $0.55 \leq \alpha \leq 1.4$. The minimum MTOW occurs at $\alpha = 0.65$. A carpet plot analysis was performed to visualize the impact of $\alpha = 0.65$ on MTOW and fuel weight. Figure 5 plots wing planform area on the abscissa and aspect ratio on the ordinate. It shows variations in MTOW of 500-lb steps by the color contours and fuel weight of 500-lb steps by the isocontour lines.

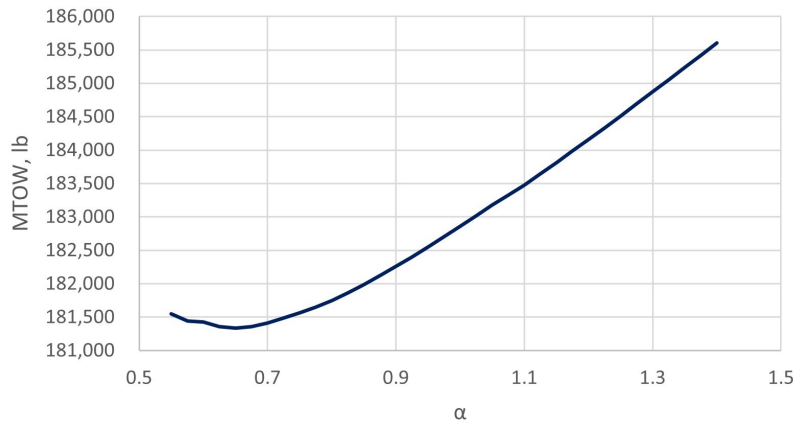


Fig. 4 Impact of HEX-fan area ratio on MTOW

A key constraint of the CHEETA aircraft is to have a wingspan less than 136 feet [12], depicted by the purple line running through the middle of Figure 5. An area of nearly constant weight, depicted in blue, exists under the wingspan constraint, indicating a wide array of configurations with similar MTOW. Unlike the previous study [12], the lowest MTOW configurations are located at wingspans below the constraint, which is due to a global reduction in MTOW and fuel requirement, caused by the reduction in peak power requirement due to reduced HEX drag. The lower peak power reduced the required number of fuel cell stacks (recall that stacks can be added in parallel to increase power output at a fixed voltage), driving reductions in MTOW and fuel weight. These results are summarized in Table 2, labelled as the isolated HEX configuration.

There is a large (79%) variation in power demand on the fuel cell throughout the design mission. Phases of flight that correspond to maximum thrust, such as take-off and top-of-climb, also correspond to maximum heat production and HEX drag. Table 2 shows the magnitude of heat load at different conditions for the baseline [12] and isolated HEX configurations. In the baseline assessment, thermal system drag was approximated as the product of HEX pressure drop and face area. This approximation overestimates thermal system drag at all phases of flight.

Given that fuel cells operate more efficiently at low power conditions, it may be advantageous to oversize the fuel cell system to improve stack efficiency and reduce fuel consumption. We define a power factor as the scalar increase on the peak power capacity of the fuel cell system. By distributing the same total power requirement over a greater number of stacks, the power required of an individual fuel cell is decreased. However, as discussed in Section III.A, fuel cells operating at a lower power are more efficient, and therefore generate less heat. This relationship can be seen in Table 2 when comparing the isolated configuration to its oversized fuel cell configuration. Equation 8 shows the thrust due to heat addition exceeds the core drag at high flight speeds. Oversized fuel cell stacks operating more efficiently thus produce less heat-induced thrust at a given power, ultimately increasing HEX drag. Therefore, the optimum oversized fuel cell system is achieved by balancing improvements in stack efficiency with reductions in radiator propulsive efficiency.

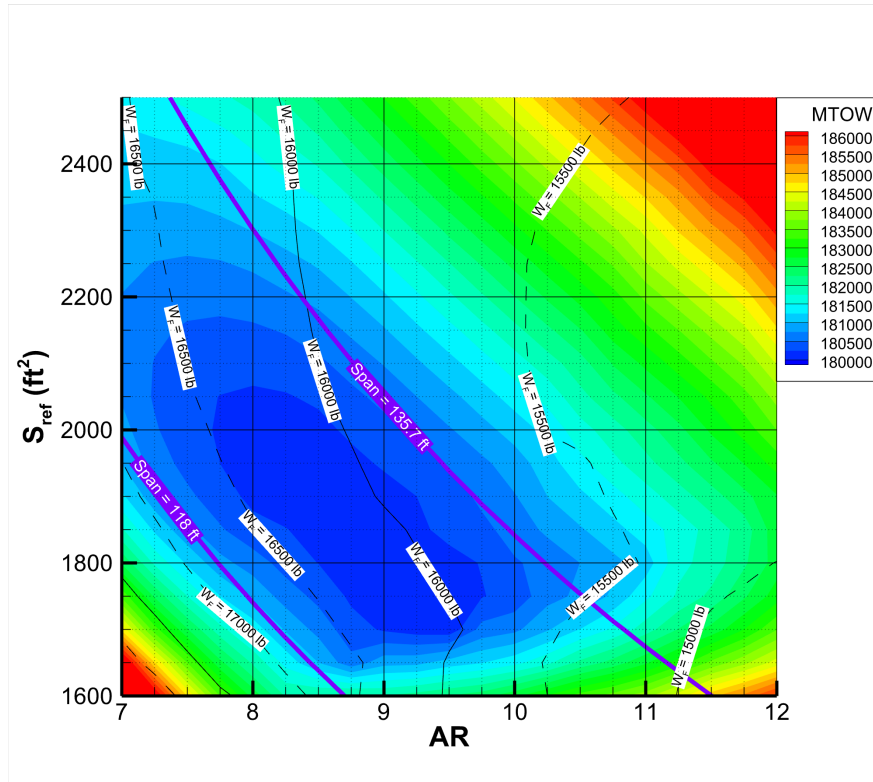


Fig. 5 Carpet plot of CHEETA with isolated heat exchangers of $\alpha = 0.65$ with dashed-line contours of required fuel weight.

Table 2 Heat load on CHEETA configurations throughout the flight

	Baseline			Isolated HEX			Isolated HEX, Oversized FC		
α	2.4			0.65			0.75		
Power Factor	1			1			1.2		
Phase of Flight	Heat	HEX Drag	% of Total Drag	Heat	HEX Drag	% of Total Drag	Heat	HEX Drag	% of Total Drag
Take-Off	15.3 MW	3,026 lb	20.7%	12.0 MW	845 lb	4.6%	15.8 MW	905 lb	7.4%
Top of Climb	15.9 MW	3,459 lb	26.1%	12.5 MW	758 lb	2.9%	16.4 MW	638 lb	6.2%
Cruise	8.51 MW	1,025 lb	9.7%	9.54 MW	110 lb	3.0%	8.42 MW	544 lb	5.2%
Descent	1.43 MW	2 lb	0.0%	1.12 MW	647 lb	10.0%	1.47 MW	1,209 lb	11.2%
Loiter	6.26 MW	296 lb	2.7%	7.40 MW	507 lb	8.1%	6.80 MW	1,250 lb	10.6%

Despite the increased HEX drag, the fuel cell efficiency gain leads to a reduction in fuel consumption, as in Table 3. To characterize this effect on HEX sizing, power factors that oversize the fuel cells are displayed with a range of HEX α -values in Figure 6. As before, changes in MTOW are in 500-lb steps shown by color contour while changes in fuel weight are in 500-lb steps shown by isocountour lines. The minimum fuel edges are highlighted in orange, with the global minimum fuel configuration indicated by a black triangle. Oversizing of the fuel cell, coupled with an increase in HEX area, enables a decrease in fuel consumption despite increased MTOW and fuel cell weight. In comparison to a Boeing 737-800 for an equivalent mission, the isolated HEX configuration consumes 4% less fuel energy, and the isolated HEX configuration with an oversized fuel cell consumes 9% less fuel energy.

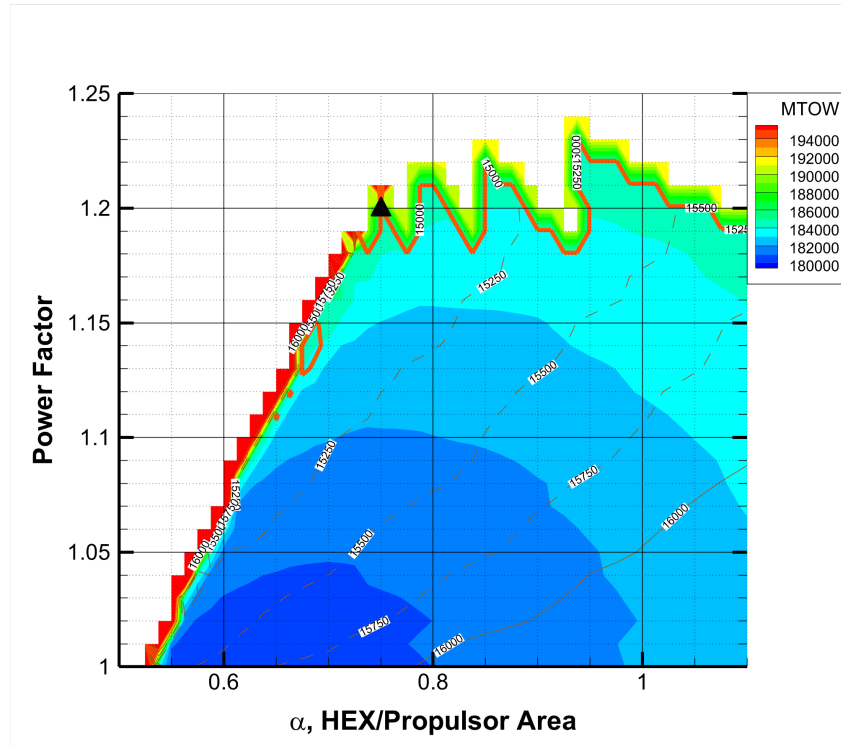


Fig. 6 Impact of HEX-fan area ratio and fuel cell oversizing on MTOW is shown with dashed-line contours of fuel weight. The global minimum of required fuel weight is indicated by a black triangle.

Table 3 Comparison of baseline and isolated HEX configurations with and without oversized fuel cells

Aircraft Parameter	Baseline	Isolated HEX	% Change from Baseline	Isolated HEX, Oversized FC	% Change from Isolated HEX
Power Factor	1.0	1.0	-	1.2	-
α	2.4	0.65	-27.08%	0.75	+15.38%
OEW	138,580 lb	129,853 lb	-6.30%	135,128 lb	+4.06%
MTOW	190,448 lb	180,613 lb	-5.16%	185,141 lb	+2.51%
Fuel Weight	16,868 lb	15,760 lb	-6.57%	15,013 lb	-4.74%
Fuel Cell Weight	20,073 lb	15,713 lb	-21.72%	20,701 lb	+31.74%
Fuel Cell Maximum Power	22 MW	17 MW	-22.73%	23 MW	+35.29%

V. Integrated Thermal/Propulsion Systems

The isolated heat exchanger is only one of several configurations that could be installed, and in this section, we examine others using a basic incompressible 1-D flow model. Three integrated configurations are shown in Figure 7. The intent is to assess the impact of varied HEX face area as well as different design choices (e.g. fan before HEX, HEX before fan, multiple flow paths) on system performance, to inform future work towards an optimal CHEETA thermal management system. In the following subsections, we consider integrated thermal propulsors in series (fan and HEX share a flow path) and in parallel (fan and HEX have separate flow paths) in the context of the baseline and isolated HEX configurations.

A. Series-integrated Thermal Propulsor

Figure 7a and 7b show configurations with a fan and heat exchanger integrated in the same duct with a shared flow path. Potential benefits include reduced nacelle wetted area for decreased nacelle drag, attenuated inlet flow distortion

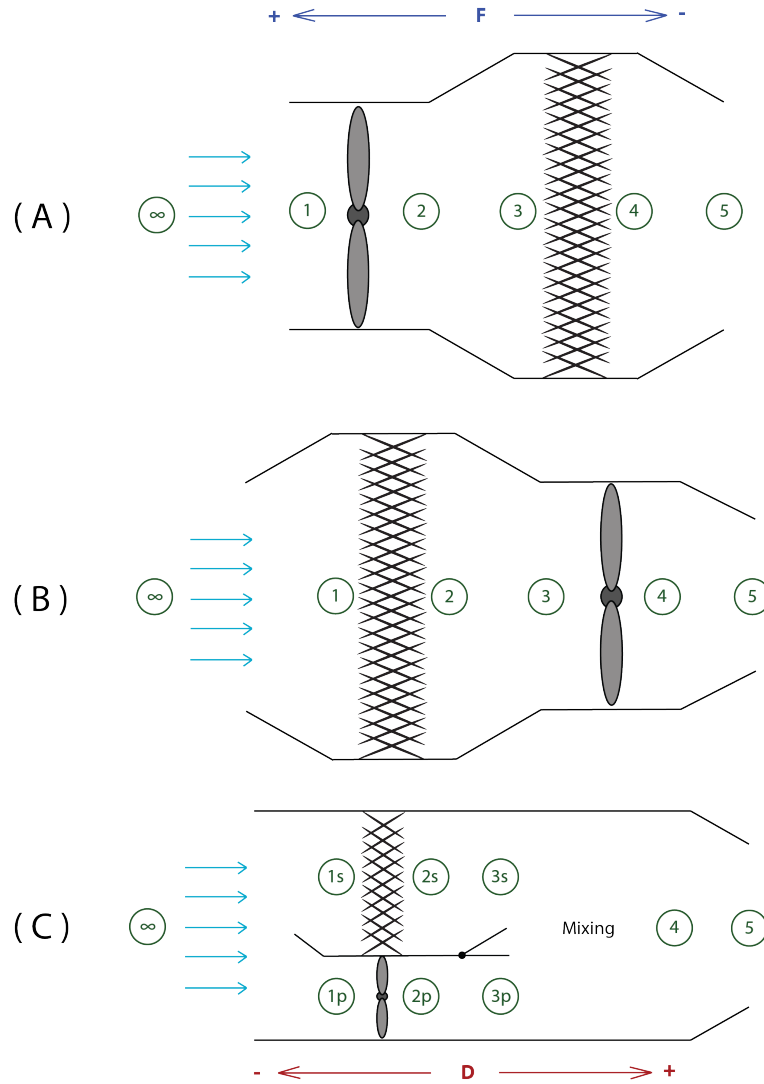


Fig. 7 Notional 1-D flow representations of a) fan-HEX series-integrated, b) HEX-fan series-integrated, and c) parallel-integrated thermal propulsors, where series-integrated entails a shared thermal/propulsion flow path and parallel-integrated entails a split flow path with a secondary cooling flow entrained by the primary fan flow

through the screen-like influence of a HEX upstream of the fan, and augmented thrust due to heat addition. Two notional 1-D flow representations of a heat exchanger and fan integrated in series are shown, with the model presented below for a fan upstream of the heat exchanger.

We can connect flow conditions between stations using Bernoulli's equation and a stagnation pressure change (ΔP):

$$P_{\infty} + \frac{1}{2}\rho u_{\infty}^2 = P_3 + \frac{1}{2}\rho_3 u_3^2 + \Delta P_{fan} \quad (16)$$

$$P_3 + \frac{1}{2}\rho u_3^2 = P_5 + \frac{1}{2}\rho_4 u_5^2 + \Delta P_{HEX} \quad (17)$$

Continuity for these stations is:

$$\dot{m} = \rho u_1 A_1 = \rho u_2 A_2 = \rho u_3 A_3 = \rho_4 u_4 A_4 = \rho_4 u_5 A_5 \quad (18)$$

In the case of the heat exchanger, we showed that the pressure drop scales with the flow velocity in Equation 9, which varies with operating conditions, as in Equation 12. Additionally, from Equation 6, the HEX effectiveness (ϵ) varies

with operating condition [14]. Importantly, this effectiveness sets the temperature rise of the working fluid over the HEX, which is responsible for the change in air density.

$$\epsilon \dot{m} C_p (T_r - T_\infty) = \dot{m} C_p (T_4 - T_\infty) \quad (19)$$

As with the isolated propulsor, the thrust is set at the aircraft level. Based on this value, we can determine the required shaft power (\dot{W}_{shaft}) using the thrust equation and the mechanical flow power (\dot{W}_K) through the duct.

$$\Sigma F_x = F_{thrust} - D_{nacelle} = \dot{m}(u_5 - u_\infty) \quad (20)$$

$$\dot{W}_K = \eta_{fan} \dot{W}_{shaft} = \frac{\dot{m} \Delta P_{fan}}{\rho} \quad (21)$$

Non-dimensionalizing the thrust and power of a series-integrated thermal propulsor,

$$C_x = \frac{2 \Sigma F_x}{\rho u_\infty^2 A_{fan}} = 2 \left(\frac{u_1}{u_\infty} \right) \left(\frac{u_5}{u_\infty} - 1 \right) - C_{nacelle} \quad (22)$$

$$C_{nacelle} = \frac{2 D_{nac}}{\rho u_\infty^2 A_1} = \alpha C_d \quad (23)$$

$$K_p = \frac{2 \dot{W}_K}{\rho u_\infty^3 A_{fan}} = \frac{2 \Delta P_{fan}}{\eta_{fan} \rho u_\infty^2} \left(\frac{u_1}{u_\infty} \right) \quad (24)$$

We assessed the impact of the HEX-fan area ratio (α) on the axial force coefficient (C_x) and power coefficient (K_p) of the series-integrated propulsors in Figure 7a and 7b. The HEX effectiveness was set as $\epsilon = 0.45$, the non-dimensional HEX pressure drop ($\Phi = 20$) based on the upper range of typical devices [15], the radiator temperature ($T_r = 180^\circ C$) based on high-temperature fuel cell operation [9], and the nacelle drag coefficient ($C_d = 0.04$) based on experiments by Robinson *et al* [24].

Figure 8 shows non-dimensional net thrust per unit power, analogous to propulsive efficiency, for a range of α -values alongside cruise and top-of-climb design points for the baseline and isolated configurations. For all α , the series-integrated thermal propulsor performs much worse. The cruise K_p of the baseline and isolated configurations is only enough to overcome the drag of the series-integrated configuration, and the integrated system requires twice the power of an isolated configuration to achieve the same net thrust. We can also see that the power required to achieve a certain thrust is slightly higher for an upstream HEX. This effect is due to the reduction in air density, due to the temperature rise from heat addition, which results in the fan requiring a larger input work for a specific pressure rise.

B. Parallel-integrated Thermal Propulsor

Another thermal system is a parallel-integrated configuration, which has a primary (p) fan stream and a secondary HEX stream (s), as shown in the 1-D flow diagram in Figure 7c. In practice, the primary and secondary streams would be arranged annularly within the duct, so the secondary stream is entrained by the primary stream of flow over the fan. We need to ensure enough air flows through the secondary stream to cool the fuel cell at any operating condition, and this is done using variable internal geometry where the secondary stream exhausts to the mixing chamber. We can relate the mechanical power of the fan to the heat rejected by the fuel cell using Equation 25.

$$\frac{\dot{m}_p \Delta P_{fan}}{\eta_{fan} \rho} = \dot{W}_K = \eta_{overall} \dot{W}_{fc} = \eta_{overall} \left(\frac{\eta_{fc}}{1 - \eta_{fc}} \right) \dot{Q} = \eta_{overall} \left(\frac{\eta_{fc}}{1 - \eta_{fc}} \right) \epsilon \dot{m}_s C_p (T_r - T_\infty) \quad (25)$$

As previously stated, we can write

$$P_\infty + \frac{1}{2} \rho u_\infty^2 = P_3 + \frac{1}{2} \rho u_{3p}^2 + \Delta P_{fan} \quad (26)$$

$$P_\infty + \frac{1}{2} \rho u_\infty^2 = P_3 + \frac{1}{2} \rho_{3s} u_{3s}^2 + \Delta P_{HEX} \quad (27)$$

The changes in density or geometry on flow velocity are given from continuity, where

$$\dot{m}_p = \rho u_{1p} A_{fan} = \rho u_{2p} A_{fan} = \rho u_{3p} A_{fan} \quad (28)$$

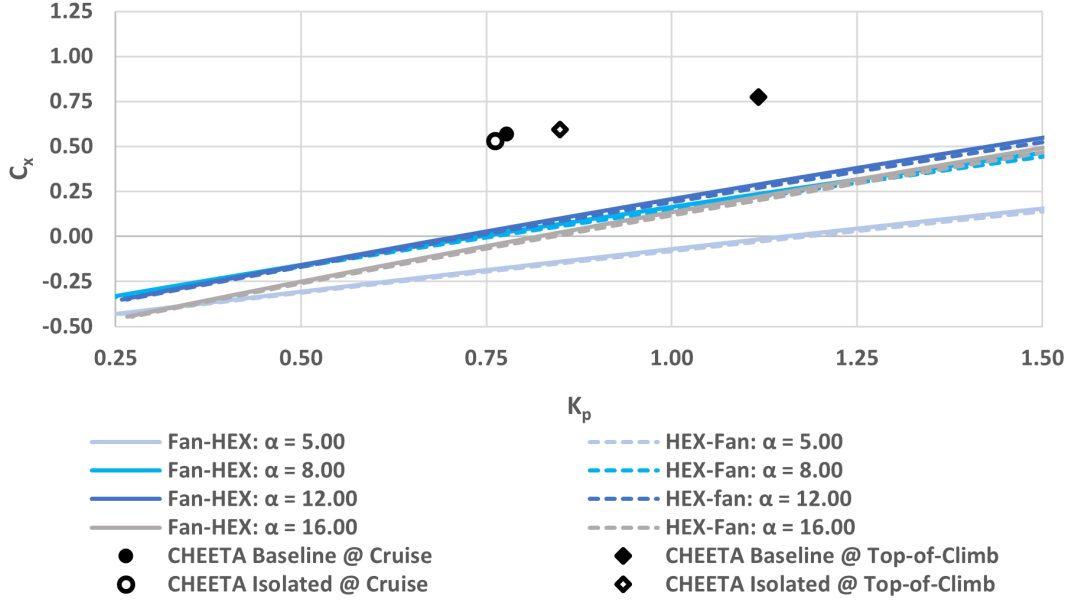


Fig. 8 For a series-integrated configurations, the optimal HEX-to-fan area ratio is bounded by increasing core drag at low area ratios and increasing external nacelle drag at high area ratios.

$$\dot{m}_s = \rho u_{1s} A_{1s} = \rho_{2s} u_{2s} A_{2s} = \rho_{2s} u_{3s} A_{3s} \quad (29)$$

The temperature rise of the working fluid over the HEX is given from the HEX effectiveness [14].

$$\epsilon \dot{m}_s C_p (T_r - T_\infty) = \dot{m}_s C_p (T_{2s} - T_\infty) \quad (30)$$

The primary and secondary streams meet at station 3, with the streams assumed to be uniformly mixed by station 4. Continuity, conservation of energy, and conservation of momentum characterize this mixing process.

$$\dot{m} = \dot{m}_p + \dot{m}_s = (\rho u_{1p} A_{1p}) + (\rho u_{1s} A_{1s}) = \rho_4 u_4 A_4 \quad (31)$$

$$\dot{m}_s C_p T_{3s} + \dot{m}_p C_p T_{3p} = \dot{m}_4 C_p T_4 \approx \dot{m}_s C_p T_{3s} + \dot{m}_p C_p T_\infty \quad (32)$$

$$P_4 A_4 - P_3 A_{3s} - P_3 A_{3p} = \dot{m}_s (u_{3s} - u_4) + \dot{m}_p (u_{3p} - u_4) \quad (33)$$

The flow at the duct exit is given by

$$\dot{m} = \rho_4 u_4 A_4 = \rho_5 u_5 A_5 \quad (34)$$

$$P_4 + \frac{1}{2} \rho_4 u_4^2 = P_5 + \frac{1}{2} \rho_5 u_5^2 \quad (35)$$

As with the series-integrated configuration, we can determine the required shaft power for given thrust requirements.

$$\Sigma F_x = F_{thrust} - D_{nacelle} = \dot{m} (u_5 - u_\infty) \quad (36)$$

$$\dot{W}_K = \eta_{fan} \dot{W}_{shaft} = \frac{\dot{m}_p \Delta P_{fan}}{\rho} \quad (37)$$

Non-dimensionalizing the thrust and power of a parallel-integrated thermal propulsor, we find

$$C_x = \frac{2 \Sigma F_x}{\rho u_\infty^2 A_{fan}} = 2 \left(\frac{A_{3s}}{A_{fan}} + 1 \right) \left(\frac{T_4}{T_\infty} \right)^{-1} \left(\frac{u_4}{u_\infty} \right) \left(\frac{u_5}{u_\infty} - 1 \right) - C_{nacelle} \quad (38)$$

$$C_{nacelle} = \frac{2 D_{nac}}{\rho u_\infty^2 A_{1p}} = (\alpha + 1) C_d \quad (39)$$

$$K_p = \frac{2\dot{W}_K}{\rho u_\infty^3 A_{fan}} = \frac{2\Delta P_{fan}}{\eta_{fan} \rho u_\infty^2} \left(\frac{u_{1p}}{u_\infty} \right) \quad (40)$$

As with the series-integration configuration, we assessed the impact of the HEX-fan area ratio (α) on the axial force coefficient (C_x) and power coefficient (K_p). The following assumptions were made: stack efficiency, $\eta_{fc} = 0.60$, HEX effectiveness, $\epsilon = 0.60$, non-dimensional HEX pressure drop ($\Phi = 20$) based on the upper range of typical devices [15], radiator temperature ($T_r = 180^\circ\text{C}$) based on fuel cell data [9], and the nacelle drag coefficient ($C_d = 0.04$) based on experiments by Robinson *et al* [24].

In Figure 9, we can see C_x begin to decrease beyond a certain K_p for low α -values ($\alpha \leq 2.00$, for the range of K_p considered). This effect is due to the larger thermal load at high power conditions, necessitating a higher secondary flow rate. For these low α cases, the elevated flow rate corresponds to high flow velocity, thus increasing pressure drop and therefore core drags. For large α , HEX pressure drop is reduced, lessening the core drag, and increasing the range of useful K_p . As with the series-integrated configuration, the external nacelle drag serves as an upper bound, limiting thrust-producing configurations to $\alpha \leq 16.00$ for this application.

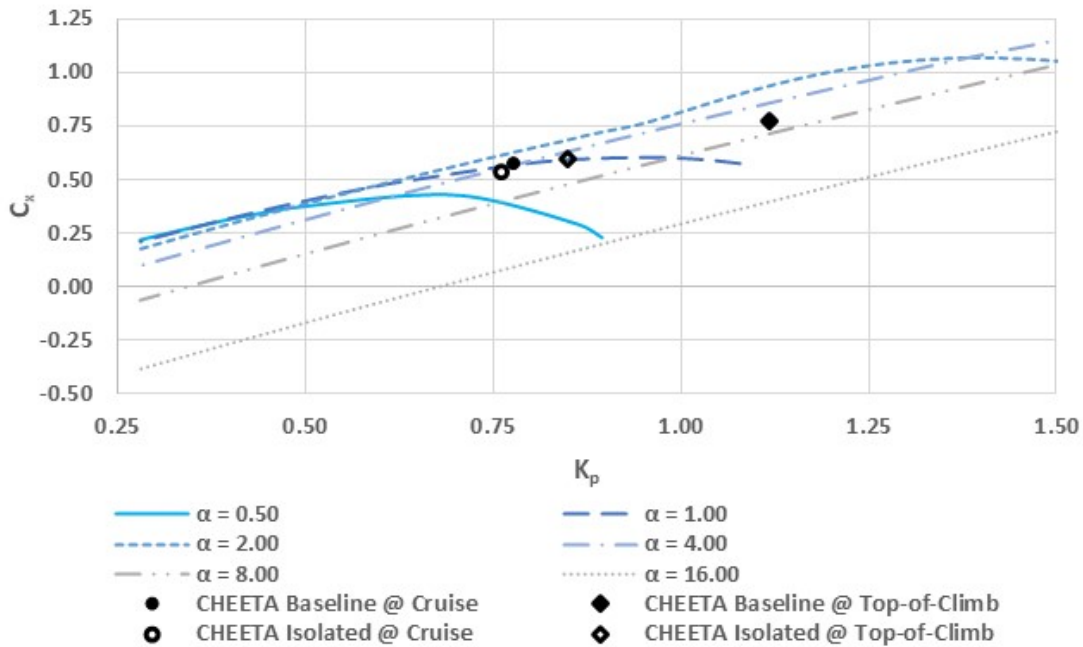


Fig. 9 Axial force coefficient is plotted versus power coefficient for a parallel-integrated thermal propulsor. The range of non-dimensional power at a specific HEX-fan area ratio (α) is limited by the airflow the HEX can pass before core drag becomes excessive. This range can be overly restrictive for low area ratios ($\alpha \leq 1.00$).

The optimal α for the parallel-integrated thermal propulsor is between 0.5 and 2.0, depending on the stack efficiency, cruise power required, and thrust required at top-of-climb. Relative to the series-integrated propulsor, these results highlight the importance of limiting airflow over the HEX to only what is required for cooling.

This configuration performs comparably to the isolated configuration, which is unsurprising since the only practical difference is the mixing of primary and secondary flows in the parallel case. Notably, the optimal α -values for the parallel-integrated propulsor are slightly larger than that of the isolated configuration. This result is primarily due to our conservative estimate of non-dimensional pressure drop, taking the upper range of typical values ($5 \leq \Phi \leq 20$) [15]. Secondly, considering compressible effects, the air density would be slightly higher throughout the system due to the ram effect, via Equation 12, enabling a reduction in HEX face area, via Equation 29, and work required from the fan, via Equation 37. Regardless, these results indicate that a parallel-integrated thermal propulsor is feasible, but a compressible assessment is required to fully characterize the performance of such a system.

VI. Conclusions and Future Work

The reduction in thermal system drag due to heat addition reduced overall power requirements at the sizing point (top-of-climb), enabling a reduction in power system size. In other words, decreased stack efficiency caused an increase in propulsive efficiency. This "coupled" effect enables an aircraft with lower MTOW, power requirements, and fuel consumption for the same mission relative to the baseline aircraft, indicating that the propulsive contribution of the thermal system must be considered when sizing the power system. Thermal system design for MW-scale electric aircraft thus cannot be considered as a simple drag penalty to be quantified after preliminary design is complete: power, propulsion, and thermal systems must be designed together.

Our assessment shows the benefit of placing the HEX downstream of the fan as well as the drag penalties of passing excessive flow over the HEX. Our inference is that an optimal thermal system design would be a bypass configuration, as in Figure 10, with variable internal geometry to control the entrained secondary airflow rate. Future work will focus on the development of a higher-fidelity flow model to be incorporated in our aircraft sizing model and an aircraft design optimization framework.

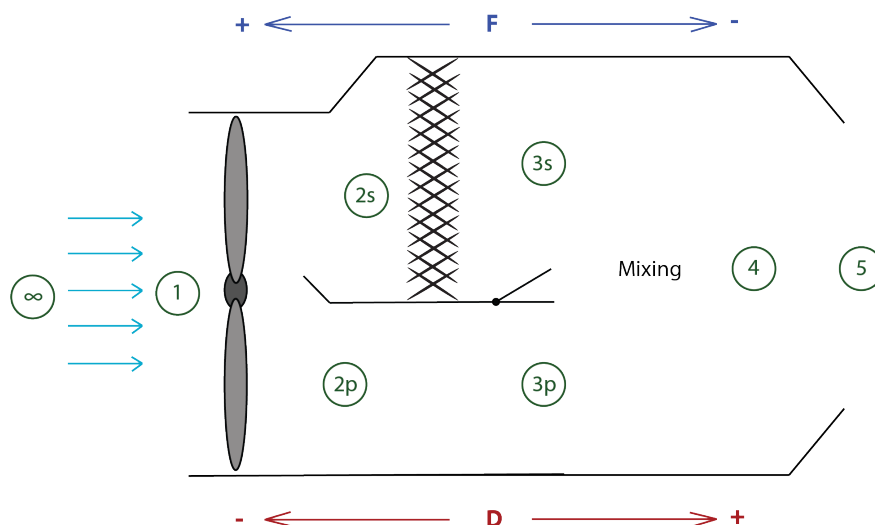


Fig. 10 Notional 1-D flow representation of a bypass-integrated thermal propulsor

VII. Appendix

The complete fuel cell component model can be found on GitHub. This repository includes an Appendix.pdf file that describes the physics of the fuel cell, the sources used to develop the model, and a comparison with experimental studies in the literature. Several MatLab scripts are included which demonstrate the implementation of the model for use in aircraft performance studies. The repository can be found here: https://github.com/cheetaillinois/Fuel_Cell_Public

Acknowledgments

This work was supported by NASA under award number 80NSSC19M0125 as part of the Center for High-Efficiency Electrical Technologies for Aircraft (CHEETA). This material is based upon work supported by the National Science Foundation Graduate Research Fellowship under Grant No. 1745302. Any opinion, findings, and conclusions or recommendations expressed in this material are those of the author(s) and do not necessarily reflect the views of the National Science Foundation. Special thanks are extended to Chellappa Balan, James Falcone, and Mike Stoia of The Boeing Company and Wolfgang Stautner of General Electric Global Research, for their contributions to hydrogen fuel cell and liquid hydrogen storage design, respectively.

References

- [1] Annapragada, S. R., MacDonald, M., Sur, A., Mahmoudi, R., and Lents, C., "Hybrid Electric Aircraft Battery Heat Acquisition System," *2018 AIAA/IEEE Electric Aircraft Technologies Symposium, EATS 2018*, Institute of Electrical and Electronics Engineers Inc., 2018, pp. 1–13. <https://doi.org/10.2514/6.2018-4992>.
- [2] Friedrich, K. A., Kallo, J., Schirmer, J., and Schmitthals, G., "Fuel Cell Systems for Aircraft Application," *ECS Transactions*, Vol. 25, No. 1, 2019, pp. 193–202. <https://doi.org/10.1149/1.3210571>.
- [3] Chandel, D., Greitzer, E. M., Hall, D. K., Reband, J., Balachandran, T., Xiao, J., and Haran, K. S., "Conceptual Design of Distributed Electrified Boundary Layer Ingesting Propulsors for the CHEETA Aircraft Concept," *AIAA Propulsion and Energy Forum*, AIAA, Virtual Event, 2021, pp. 1–16. <https://doi.org/10.2514/6.2021-3287>.
- [4] Blanding, D., "Subsystem design and integration for the more electric aircraft," *ICAS-Secretariat - 25th Congress of the International Council of the Aeronautical Sciences 2006*, Vol. 6, 2006, pp. 3732–3739. <https://doi.org/10.2514/6.2007-4828>.
- [5] Rheume, J. M., and Lents, C. E., "Design and Simulation of a Commercial Hybrid Electric Aircraft Thermal Management System," *2018 AIAA/IEEE Electric Aircraft Technologies Symposium, EATS 2018*, Institute of Electrical and Electronics Engineers Inc., 2018, pp. 1–9. <https://doi.org/10.2514/6.2018-4994>.
- [6] Rheume, J. M., and Lents, C. E., "Commercial hybrid electric aircraft thermal management system design, simulation, and operation improvements," *AIAA Propulsion and Energy Forum and Exposition, 2019*, American Institute of Aeronautics and Astronautics Inc, AIAA, 2019, pp. 1–23. <https://doi.org/10.2514/6.2019-4492>.
- [7] Kerrebrock, J. L., *Aircraft Engines and Gas Turbines*, MIT Press, Cambridge, MA, 1992.
- [8] Pratt, J. W., Klebanoff, L. E., Munoz-Ramos, K., Akhil, A. A., Curgus, D. B., and Schenkman, B. L., "Proton exchange membrane fuel cells for electrical power generation on-board commercial airplanes," *Applied Energy*, Vol. 101, No. May, 2013, pp. 776–796. <https://doi.org/10.1016/j.apenergy.2012.08.003>.
- [9] Tang, H., Geng, K., Wu, L., Liu, J., Chen, Z., You, W., Yan, F., Guiver, M. D., and Li, N., "Fuel cells with an operational range of -20°C to 200°C enabled by phosphoric acid-doped intrinsically ultramicroporous membranes," *Nature Energy*, 2022. <https://doi.org/10.1038/s41560-021-00956-w>.
- [10] Welstead, J., Felder, J., Guynn, M., Haller, B., Tong, M., Jones, S., Ordaz, I., Quinlan, J., and Mason, B., "Overview of the NASA STARC-ABL (Rev. B) Advanced Concept," *One Boeing NASA Electric Aircraft Workshop*, 2017. URL <https://ntrs.nasa.gov/search.jsp?R=20170005612>.
- [11] Sozer, E., Maldonado, D., Bhamidipati, K., and Schnulo, S. L., "Computational evaluation of an oml-based heat exchanger concept for heather," *AIAA Propulsion and Energy 2020 Forum*, American Institute of Aeronautics and Astronautics Inc, AIAA, 2020, pp. 1–22. <https://doi.org/10.2514/6.2020-3575>.
- [12] Waddington, E., Merret, J. M., and Ansell, P. J., "Impact of LH 2 Fuel Cell-Electric Propulsion on Aircraft Configuration and Integration," *AIAA Aviation Forum*, American Institute of Aeronautics and Astronautics (AIAA), Virtual Event, 2021, pp. 1–18. <https://doi.org/10.2514/6.2021-2409>.
- [13] Meredith, F., "Cooling of Aircraft Engines with Special Reference to Ethylene Glycol Radiators Enclosed in Ducts," Tech. rep., Aeronautical Research Committee Reports and Memoranda No. 1683, London, 1935.
- [14] Kays, W. M., and London, A. L., *Compact Heat Exchangers*, 3rd ed., McGraw-Hill, New York, 1984.
- [15] Drela, M., "Aerodynamics of heat exchangers for high-altitude aircraft," *Journal of Aircraft*, Vol. 33, No. 1, 1996, pp. 176–184. <https://doi.org/10.2514/3.46919>.
- [16] Larminie, J., and Dicks, A., *Fuel Cell Systems Explained*, 2nd ed., Wiley, Chichester, England, 2003. <https://doi.org/10.1002/9781118878330>.
- [17] Hirschenhofer, J. H., Stauffer, D. B., Engleman, R. R., and Klett, M. G., "Fuel cell handbook (DOE/FETC-99/1076)," Tech. rep., U.S. Department of Energy, 1998. URL <https://www.osti.gov/biblio/14997-fuel-cell-handbook-fourth-edition>.
- [18] Nehrir, M. H., and Wang, C., *Modeling and Control of Fuel Cells*, Wiley, Hoboken, New Jersey, USA, 2009.
- [19] Tafel, J., "About the polarization during cathodic hydrogen evolution," *Z. phys. Chem*, Vol. 50, 1905, p. 641.
- [20] Sampson, B., "Hydrogen fuel cell plant opens in UK," *Aerospace Testing International*, 2022. URL <https://www.aerospacetestinginternational.com/features/hydrogen-fuel-cell-plant-opens-in-uk.html>.

- [21] Warwick, G., “MTU Sets Zero-Emission Sights On Hydrogen Fuel-Cell Propulsion,” *Aviation Week*, 2022. URL <https://aviationweek.com/aerospace/aircraft-propulsion/mtu-sets-zero-emission-sights-hydrogen-fuel-cell-propulsion>.
- [22] Dynalene, “Properties of Dynalene PEG Fluids,” Tech. rep., Dynalene, Inc., Whitehall, PA, USA, 2018. URL https://www.dynalene.com/wp-content/uploads/2018/07/Dynalene_PEG_Series_Technical_Data_Sheet.pdf.
- [23] Greitzer, E. M., Tan, C. S., and Graf, M. B., *Internal Flow: Concepts and Applications*, Cambridge Engine Technology Series, Cambridge University Press, 2004. <https://doi.org/10.1017/CBO9780511616709>.
- [24] Robinson, M., MacManus, D. G., and Sheaf, C., “Aspects of aero-engine nacelle drag,” *Proceedings of the Institution of Mechanical Engineers, Part G: Journal of Aerospace Engineering*, Vol. 233, No. 5, 2019, pp. 1667–1682. <https://doi.org/10.1177/0954410018765574>.
- [25] Balan, C., “Private Communication,” , 2020.
- [26] Roskam, J., *Airplane Design Part V: Component Weight Estimation*, Roskam Aviation and Engineering Corporation, Ottawa, Kansas, 1985.